Soft Matter

Modeling high strain-rate microcavitation in soft materials: The role of material behavior in bubble dynamics

Journal:	*Soft Matter*
Manuscript ID	SM-ART-09-2022-001212.R1
Article Type:	Paper
Date Submitted by the Author:	09-May-2023
Complete List of Authors:	Tzoumaka, Anastasia; Brown University, School of Engineering Yang, Jin; University of Wisconsin-Madison, Department of Mechanical Engineering; The University of Texas at Austin, Department of Aerospace Engineering and Engineering Mechanics Buyukozturk, Selda; Brown University, School of Engineering; University of Wisconsin-Madison, Department of Mechanical Engineering Franck, Christian; University of Wisconsin-Madison, Department of Mechanical Engineering Henann, David; Brown University, School of Engineering

Soft Matter

ARTICLE TYPE

Cite this: DOI: 00.0000/xxxxxxxxxx

Modeling high strain-rate microcavitation in soft materials: The role of material behavior in bubble dynamics

Anastasia Tzoumaka,[a] Jin Yang,[b,c] Selda Buyukozturk,[a,b] Christian Franck[b] and David L. Henann*[a]

Received Date
Accepted Date

DOI: 00.0000/xxxxxxxxxx

Inertial Microcavitation Rheometry (IMR) is a promising tool for characterizing the mechanical behavior of soft materials at high strain rates. In IMR, an isolated, spherical microbubble is generated inside a soft material, using either a spatially-focused pulsed laser or focused ultrasound, to probe the mechanical behavior of the soft material at high strain rates ($> 10^3\ s^{-1}$). Then, a theoretical modeling framework for inertial microcavitation, incorporating all the dominant physics, is used to extract information regarding the mechanical behavior of the soft material by fitting model predictions to the experimentally measured bubble dynamics. To model the cavitation dynamics, approaches based on extensions of the Rayleigh-Plesset equation are commonly used; however, these approaches cannot consider bubble dynamics that involves appreciable compressible behavior and place a limit on the nonlinear viscoelastic constitutive models that may be employed to describe the soft material. To circumvent these limitations, in this work, we develop a finite-element-based numerical simulation capability for inertial microcavitation of spherical bubbles that enables appreciable compressibility to be accounted for and more complex viscoelastic constitutive laws to be incorporated. We first apply the numerical simulation capability to understanding the role of material compressibility during violent spherical bubble collapse, and based on finite-element simulations, we propose a Mach-number-based threshold of 0.08, beyond which bubble collapse is violent, and the bubble dynamics involves compressibility not accounted for in Rayleigh-Plesset-based approaches. Second, we consider more complex viscoelastic constitutive models for the surrounding material, including nonlinear elastic and power-law viscous behavior, and apply IMR by fitting computational results to experimental data from inertial microcavitation of polyacrylamide (PA) gels in order to determine material parameters for PA gels at high strain rates.

1 Introduction

Soft materials–such as biological tissues and gels used as tissue phantoms–undergoing high strain-rate deformation play a crucial role in a number of important engineering problems–e.g., modeling head injuries due to blunt impact and blast[1–4], estimating tissue damage during histotripsy procedures[5–7], and understanding the physics involved in laser-based surgical procedures[8,9]. Therefore, there is a need for mechanical characterization of soft materials at high strain rates ($> 10^3\ s^{-1}$). While low-to-moderate strain-rate (10^{-4}–$10^2\ s^{-1}$) testing techniques–such as tension-compression experiments, indentation[10], needle-induced cavitation[11,12], and volume-controlled cavity expansion[13–15]–have been successfully deployed to understand the mechanical behavior of soft materials, applying traditional high-strain-rate material characterization techniques–e.g., Kolsky bar[16] or plate-impact testing[17]–to soft materials remains challenging, due to their low impedance and slow shear wave speeds.

To address this challenge, significant effort in recent years has gone towards developing new characterization techniques capable of extracting information on the high strain-rate mechanical behavior of soft materials–including small-scale ballistic cavitation[18], laser-induced particle impact testing[19], shear impact testing[20], and Inertial Microcavitation Rheometry (IMR)[21–25], which is the focus of the present work. IMR belongs to a class of cavitation-based material characterization techniques[26]–including needle-induced cavitation[11,12,18] and volume-controlled cavity expansion[13–15]–and is unique in its ability to mechanically characterize soft materials at high strain rates greater than $10^3\ s^{-1}$. In IMR, a single spherical microbubble is generated inside a soft material using either a spatially-focused pulsed laser[21,27] or high-amplitude focused ultrasound[23,28,29], inducing high strain-rate ($> 10^3\ s^{-1}$) deformation in the surrounding material. The subsequent radius versus time behavior of the spherical bubble is measured using high-speed imaging. Then, since the bubble dynamics involves inhomogeneous deformation

[a] School of Engineering, Brown University, Providence, RI, USA. E-mail: david_henann@brown.edu
[b] Department of Mechanical Engineering, University of Wisconsin-Madison, Madison, WI, USA.
[c] Department of Aerospace Engineering and Engineering Mechanics, The University of Texas at Austin, Austin, TX, USA.

in the surrounding soft material, a cavitation modeling framework that accounts for the dominant physics, including the viscoelastic constitutive behavior of the soft material[21,22,30,31], is required. By fitting predictions of the cavitation modeling framework to the experimentally measured bubble dynamics, nonlinear viscoelastic material parameters for a given constitutive model may be inferred, and the IMR approach has been successfully applied to measuring the viscoelastic mechanical properties of polyacrylamide[21,22,27], agarose[23,25], and collagen[4] gels at high strain rates. Moreover, similar efforts involving cavitation induced by a pulsed laser have been applied to fibrin and polyethylene glycol (600) diacrylate gels[32] as well as to polydimethylsiloxane gels[33] aided by laser-absorbing seed particles.

To obtain accurate estimates of high strain-rate material properties for soft materials using IMR, a high fidelity description of the dominant physics must be incorporated into the cavitation modeling framework. Approaches based on the Rayleigh-Plesset (RP) equation[34,35] and its extensions are commonly used to describe cavitation dynamics in liquids and soft solids. In particular, the Keller-Miksis (KM) equation[36] extends the RP equation to account for slight compressibility and stress wave propagation in the surrounding material and has been used in many studies of cavitation in soft solids[21–25,27,28,30,31]. However, use of both the RP and the KM equations places several limitations on the types of constitutive behavior for the surrounding material that may be included in the cavitation modeling framework. First, since the RP equation assumes the surrounding material to be incompressible and the KM equation only accounts for slight compressibility, predictions obtained using the RP or KM equation can become inaccurate when the bubble dynamics involves appreciable material compressibility, i.e., volumetric strain magnitudes on the order of 0.01 or greater. This situation is expected to arise for violently collapsing bubbles, in which the maximum Mach number in the surrounding material is on the order of 0.1 or greater[22]. Second, the implementation of the viscoelastic, distortional material response into the RP/KM framework requires the integration of mathematical expressions, which are challenging to evaluate in closed form for sufficiently complex constitutive models. A number of nonlinear viscoelastic models have been implemented in the KM framework[22,30,31] in an effort to capture the mechanical behavior of soft materials; however, doing so remains mathematically intractable for many of the finite-deformation constitutive models utilized in the literature for soft solids[15,37,38]. Therefore, the RP/KM framework places limitations on the breadth of material behavior that may be considered to characterize the high strain-rate response of soft materials.

The purpose of this paper is to address the limitations that the use of the RP/KM equation places on IMR. We develop a numerical framework for modeling the cavitation dynamics of a single spherical bubble using the finite-element (FE) method, which enables the implementation of general constitutive models for the surrounding soft material. With this numerical tool, we incorporate a description of the compressibility of the surrounding material, which leads to a numerical framework that describes the bubble dynamics more accurately when studying violently collapsing bubbles. Furthermore, we consider more complex viscoelastic constitutive descriptions of the surrounding material, including nonlinear elastic and power-law viscous behavior, which enables a higher fidelity characterization of soft materials at high strain rates.

The remainder of this paper is organized as follows. In Section 2, we summarize the continuum field equations governing the dynamics of spherical bubbles in soft viscoelastic media, including the nonlinear, finite-deformation viscoelastic constitutive models considered in our cavitation modeling framework. In Section 3, we describe the KM-based and FE-based modeling frameworks for both laser-induced and ultrasound-induced cavitation. Section 4 compares FE-based and KM-based simulations of bubble dynamics as bubble collapse becomes increasingly violent and proposes a Mach-number-based criteria for when the bubble dynamics involves material compressibility beyond that accounted for in the KM-based approach, and Section 5 applies FE-based simulations in IMR to obtain improved high-strain-rate properties for polyacrylamide gels–specifically, using the laser-induced cavitation data of Yang *et al.* [22] and Buyukozturk *et al.* [27]. Finally, we close with some concluding remarks in Section 6.

2 Continuum framework

In this section, we summarize the continuum field equations governing the dynamics of spherical bubbles in soft viscoelastic media. We assume (1) that the bubble and the motion of the surrounding material remain spherically symmetric during the cavitation process and (2) that the surrounding material is a homogeneous, infinite, isotropic viscoelastic medium.

2.1 Kinematics

We denote the undeformed radius of the spherical bubble as R_0 and the referential radial coordinate in the surrounding material as r_0, where r_0 is measured from the center of the bubble. The reference configuration for the surrounding material is identified by the material points $\{r_0 | R_0 \leq r_0 < \infty\}$. The time-dependent bubble radius in the deformed configuration is $R(t)$, and we assume a spherically symmetric motion, in which material points r_0 deform to spatial points $r = r(r_0, t)$ (see Fig. 1). The deformation gradient tensor $\mathbf{F}$ in the spherical coordinate system is

$$[\mathbf{F}] = \begin{bmatrix} \dfrac{\partial r}{\partial r_0} & 0 & 0 \\ 0 & \dfrac{r}{r_0} & 0 \\ 0 & 0 & \dfrac{r}{r_0} \end{bmatrix}, \tag{1}$$

with the volume ratio given by $J = \det \mathbf{F} > 0$.* For a spherically symmetric motion, the only non-zero component of the displacement vector is the radial component $u_r(r_0, t) = r(r_0, t) - r_0$. The left Cauchy-Green deformation tensor is $\mathbf{B} = \mathbf{F}\mathbf{F}^\top$, the distortional deformation gradient tensor is $\bar{\mathbf{F}} = J^{-1/3}\mathbf{F}$, the distortional left Cauchy-Green deformation tensor is $\bar{\mathbf{B}} = J^{-2/3}\mathbf{B}$, and the distortional first principal stretch invariant is $\bar{I}_1 = \operatorname{tr} \bar{\mathbf{B}}$.

* *Notation:* We write $\operatorname{tr}\mathbf{A}$, $\det\mathbf{A}$, $\operatorname{dev}\mathbf{A}$, $\operatorname{sym}\mathbf{A}$, and $\operatorname{skw}\mathbf{A}$ to denote the trace, determinant, deviatoric part, symmetric part, and skew part of a tensor $\mathbf{A}$, respectively.

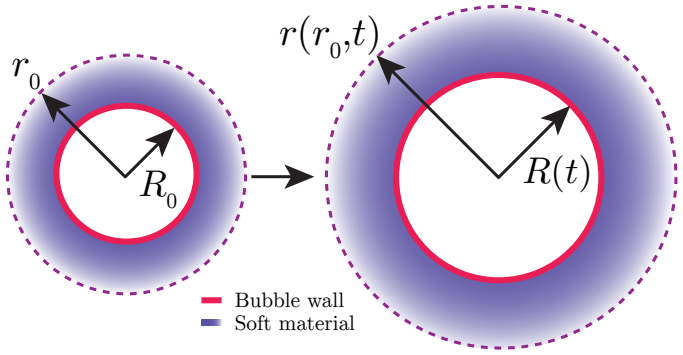

Fig. 1 Schematic representation of the reference and deformed configurations. The radial coordinates in the reference and deformed configurations are denoted as r_0 and r, and the undeformed and deformed bubble radii are R_0 and R.

The referential descriptions of the radial components of the velocity and acceleration vectors are $\dot{u}_r(r_0,t)$ and $\ddot{u}_r(r_0,t)$, respectively, where the superposed dot denotes the material time derivative. The spatial descriptions of the radial components of the velocity and acceleration vectors are $v_r(r,t)$ and $a_r(r,t)$, and the components of the spatial velocity gradient tensor $\mathbf{L}$ in the spherical coordinate system are

$$[\mathbf{L}] = \begin{bmatrix} \dfrac{\partial v_r}{\partial r} & 0 & 0 \\ 0 & \dfrac{v_r}{r} & 0 \\ 0 & 0 & \dfrac{v_r}{r} \end{bmatrix}. \tag{2}$$

Finally, the stretching and spin tensors are $\mathbf{D} = \operatorname{sym}\mathbf{L}$ and $\mathbf{W} = \operatorname{skw}\mathbf{L}$, respectively.

2.2 Viscoelastic constitutive models for the surrounding material

Previous works[21–23,25] have demonstrated that in order to accurately describe the nonlinear behavior of soft materials at high strain-rates, one must take into account both hyperelastic and viscous material behavior. In this subsection, we discuss the library of finite-deformation viscoelastic constitutive models that we have considered in our cavitation modeling framework, which fall into two categories. The first category is based on a nonlinear generalization of the Kelvin-Voigt (KV) model of linear viscoelasticity and consists of a hyperelastic response in parallel with a Newtonian rheological response, as illustrated in the rheological schematic of Fig. 2(a). We refer to this category of models as KV-type models, which are discussed in Section 2.2.1. The second category is motivated by the standard linear solid model of linear viscoelasticity and consists of a hyperelastic response in parallel with a finite-deformation Maxwell element, as illustrated in Fig. 2(b). We refer to nonlinear generalizations of the standard linear solid model as Standard Nonlinear Solids (SNS), or SNS-type models, which are discussed in Section 2.2.2.

2.2.1 KV-type models

Motivated by the Kelvin-Voigt model of linear viscoelasticity, we consider a finite-deformation viscoelastic model consisting of a

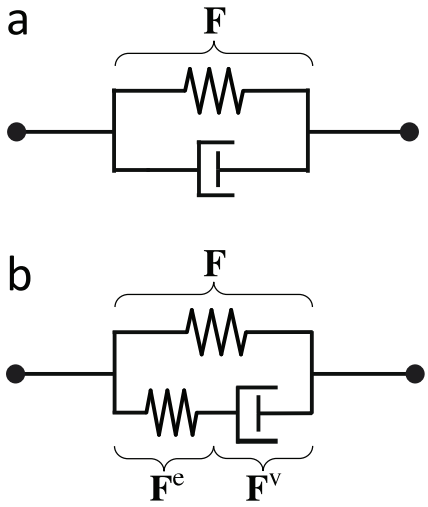

Fig. 2 Rheological schematics of the of the nonlinear, finite-deformation viscoelastic modeling approaches for (a) KV-type models and (b) SNS-type models.

hyperelastic response (top branch in Fig. 2(a)) in parallel with a Newtonian viscous response (bottom branch in Fig. 2(a)). The contributions to the Cauchy stress due to the hyperelastic response and the viscous response are denoted as $\boldsymbol{\sigma}^{\mathrm{e}}$ and $\boldsymbol{\sigma}^{\mathrm{v}}$, respectively, and the total Cauchy stress is $\boldsymbol{\sigma} = \boldsymbol{\sigma}^{\mathrm{e}} + \boldsymbol{\sigma}^{\mathrm{v}}$.

The referential free-energy density describing the hyperelastic response ψ is taken to depend upon the invariants $\bar{I}_1$ and J for slightly-compressible, isotropic materials. In order to account for strain-stiffening effects in the surrounding material, we consider a quadratic-law distortional hyperelastic response[22,39] with free-energy density given by

$$\psi = \frac{G}{2}\left[(\bar{I}_1 - 3) + \frac{\alpha}{2}(\bar{I}_1 - 3)^2\right] + \frac{K}{2}(J-1)^2, \tag{3}$$

where G is the ground-state shear modulus, α is a dimensionless parameter that describes large-deformation strain-stiffening behavior, and K is the ground-state bulk modulus. The first terms represent the free energy due to distortional (constant volume) deformation, and the last term in Eq. (3) represents the free energy due to purely volumetric deformation. Note that when $\alpha = 0$, Eq. (3) reduces to the free-energy density for a slightly-compressible Neo-Hookean material. Regarding compressibility, the ground-state bulk modulus K may be given through the longitudinal wave speed c and the ground-state shear modulus G by $K = \rho_0 c^2 - (4/3)G$, where ρ_0 is the referential mass density. For many soft viscoelastic materials, $K \gg G$, but instead of idealizing the material as incompressible, we treat the material as slightly compressible and examine the effect of compressibility on bubble dynamics in Section 4. The associated hyperelastic contribution to the Cauchy stress is then

$$\boldsymbol{\sigma}^{\mathrm{e}} = 2J^{-1}\frac{\partial \psi}{\partial \mathbf{B}}\mathbf{B} = J^{-1}G\left[1 + \alpha(\bar{I}_1 - 3)\right]\operatorname{dev}\bar{\mathbf{B}} + K(J-1)\mathbf{1}. \tag{4}$$

Neglecting volumetric viscosity, the viscous contribution to the

Cauchy stress for Newtonian rheological behavior is

$$\boldsymbol{\sigma}^{\mathrm{v}} = 2\mu\,\mathrm{dev}(\mathbf{D}), \tag{5}$$

where μ is the shear viscosity. We note that it can be difficult to incorporate more complex rheological behavior into KV-type models. In particular, rheological constitutive equations involving shear-thinning, power-law behavior or a yield stress exhibit a strain-rate dependent viscosity that diverges as the strain-rate approaches zero, which is problematic in the modeling of bubble dynamics since the strain rate approaches zero far from the bubble as $r \to \infty$. Complex rheological behavior may be more readily incorporated in SNS-type models, discussed in Section 2.2.2.

The total Cauchy stress is then

$$\boldsymbol{\sigma} = \boldsymbol{\sigma}^{\mathrm{e}} + \boldsymbol{\sigma}^{\mathrm{v}} = J^{-1} G\left[1 + \alpha(\bar{I}_1 - 3)\right]\mathrm{dev}\,\bar{\mathbf{B}} + K(J-1)\,\mathbf{1} + 2\mu\,\mathrm{dev}(\mathbf{D}). \tag{6}$$

When $\alpha > 0$, the model accounts for strain-stiffening, and we refer to this model as the *quadratic-law Kelvin-Voigt (qKV) model*. The qKV model involves the following four material parameters: the ground-state shear modulus G, the strain-stiffening parameter α, the bulk modulus K, and the shear viscosity μ. When strain-stiffening is neglected, $\alpha = 0$, and three material parameters remain. We refer to this model as the *Neo-Hookean Kelvin-Voigt (NH-KV) model*.

2.2.2 SNS-type models

SNS-type constitutive modeling approaches are based on a decomposition of the material response into an equilibrium hyperelastic response and a dissipative, non-equilibrium contribution. With reference to the schematic in Fig. 2(b), the top branch corresponds to the equilibrium hyperelastic response of the material, and the bottom branch stands for the non-equilibrium, rate-dependent material response, represented by the finite-deformation Maxwell element in parallel with the equilibrium branch.

The referential free-energy density ψ is additively decomposed into equilibrium and non-equilibrium contributions: $\psi = \psi^{\mathrm{eq}} + \psi^{\mathrm{neq}}$, and the equilibrium hyperelastic response is specified through the free-energy density ψ^{eq}, which we take to be given through Eq. (3), so that the corresponding equilibrium contribution to the Cauchy stress $\boldsymbol{\sigma}^{\mathrm{eq}}$ is in the same form as given in Eq. (4).

The non-equilibrium, rate-dependent material response is accounted for by the finite-deformation Maxwell element (Fig. 2, bottom branch). For the non-equilibrium branch, the deformation gradient $\mathbf{F}$ is multiplicatively decomposed into elastic and viscous parts: $\mathbf{F} = \mathbf{F}^{\mathrm{e}}\mathbf{F}^{\mathrm{v}}$, where $\mathbf{F}^{\mathrm{e}}$ is the non-equilibrium elastic distortion with $J^{\mathrm{e}} = \det\mathbf{F}^{\mathrm{e}} > 0$, and $\mathbf{F}^{\mathrm{v}}$ is the viscous distortion with $J^{\mathrm{v}} = \det\mathbf{F}^{\mathrm{v}} = 1$. The right polar decomposition of $\mathbf{F}^{\mathrm{e}}$ is $\mathbf{F}^{\mathrm{e}} = \mathbf{R}^{\mathrm{e}}\mathbf{U}^{\mathrm{e}}$, where $\mathbf{U}^{\mathrm{e}}$ is the elastic right stretch tensor and $\mathbf{R}^{\mathrm{e}}$ is the elastic rotation tensor, and the elastic logarithmic (Hencky) finite-strain tensor is defined as $\mathbf{E}^{\mathrm{e}} = \ln\mathbf{U}^{\mathrm{e}}$. We take the non-equilibrium free-energy density to be given by

$$\psi^{\mathrm{neq}}(\mathbf{E}^{\mathrm{e}}) = G_1|\mathrm{dev}\,\mathbf{E}^{\mathrm{e}}|^2, \tag{7}$$

where G_1 is the non-equilibrium shear modulus. The stress conjugate to the elastic logarithmic strain is referred to as the Mandel stress and is given by

$$\mathbf{M}^{\mathrm{e}} = \frac{\partial\psi^{\mathrm{neq}}}{\partial\mathbf{E}^{\mathrm{e}}} = 2G_1\,\mathrm{dev}\,\mathbf{E}^{\mathrm{e}}, \tag{8}$$

and the non-equilibrium contribution to the Cauchy stress is given through the Mandel stress by $\boldsymbol{\sigma}^{\mathrm{neq}} = J^{\mathrm{e}-1}\mathbf{R}^{\mathrm{e}}\mathbf{M}^{\mathrm{e}}\mathbf{R}^{\mathrm{e}\top}$. We note that since the non-equilibrium free-energy density, Eq. (7), only involves the deviatoric part of the elastic logarithmic strain, the consequent Mandel stress $\mathbf{M}^{\mathrm{e}}$ and non-equilibrium contribution to the Cauchy stress $\boldsymbol{\sigma}^{\mathrm{neq}}$ are both deviatoric as well, and the volumetric material response is due to the equilibrium response alone. The total Cauchy stress is then given by $\boldsymbol{\sigma} = \boldsymbol{\sigma}^{\mathrm{eq}} + \boldsymbol{\sigma}^{\mathrm{neq}}$ [40].

Neglecting viscous spin, i.e., assuming $\mathbf{W}^{\mathrm{v}} = \mathrm{skw}(\dot{\mathbf{F}}^{\mathrm{v}}\mathbf{F}^{\mathrm{v}-1}) = \mathbf{0}$, the evolution of $\mathbf{F}^{\mathrm{v}}$ is given by $\dot{\mathbf{F}}^{\mathrm{v}} = \mathbf{D}^{\mathrm{v}}\mathbf{F}^{\mathrm{v}}$, where $\mathbf{D}^{\mathrm{v}}$ is the symmetric viscous stretching tensor. Finally, it remains to specify a constitutive equation for $\mathbf{D}^{\mathrm{v}}$. Defining the non-equilibrium equivalent shear stress $\bar{\tau} = \sqrt{\mathbf{M}^{\mathrm{e}} : \mathbf{M}^{\mathrm{e}}/2}$, we adopt the following constitutive equation for $\mathbf{D}^{\mathrm{v}}$:

$$\mathbf{D}^{\mathrm{v}} = \dot{\bar{\gamma}}^{\mathrm{v}}\frac{\mathbf{M}^{\mathrm{e}}}{2\bar{\tau}} \quad \text{with} \quad \dot{\bar{\gamma}}^{\mathrm{v}} = \dot{\gamma}_0\left(\frac{\bar{\tau}}{G}\right)^{1/m}, \tag{9}$$

where $\dot{\bar{\gamma}}^{\mathrm{v}}$ denotes the equivalent shear viscous strain rate. The dimensionless material parameter $m > 0$ represents a strain-rate sensitivity exponent, and the parameter $\dot{\gamma}_0 > 0$ is a reference shear strain rate. The equilibrium ground-state shear modulus G is included in Eq. (9) as a reference shear stress for dimensional consistency. For $0 < m < 1$, the rheological behavior of the non-equilibrium response is shear thinning, and for $m = 1$, the rheological behavior is Newtonian. For the non-Newtonian case, two material parameters are required to describe the rheological response, m and $\dot{\gamma}_0$, while for the Newtonian case, only one material parameter is required: the constant shear viscosity $\mu = G/\dot{\gamma}_0$. In this case, Eq. (9) takes the form

$$\mathbf{D}^{\mathrm{v}} = \frac{\mathbf{M}^{\mathrm{e}}}{2\mu}. \tag{10}$$

The constitutive modeling approach described above accounts for viscoelastic behavior, strain-stiffening, non-Newtonian rheological behavior, and compressibility and involves the following six material parameters: the equilibrium shear modulus G, the strain-stiffening parameter α, the bulk modulus K, the non-equilibrium shear modulus G_1, the strain-rate sensitivity exponent m, and the reference strain rate $\dot{\gamma}_0$. We note that in the limit that the non-equilibrium shear modulus is much greater than the equilibrium shear modulus, i.e., $G_1/G \to \infty$, the distortional part of the non-equilibrium elastic response becomes nearly rigid, i.e., $\mathbf{F}^{\mathrm{e}} \to J^{\mathrm{e}}\mathbf{1}$, and an SNS-type model effectively reduces to a KV-type model. As pointed out in the preceding section, utilizing power-law rheological behavior in a KV-type model can be problematic, due to the diverging viscosity as the strain-rate approaches zero. Thus, taking $G_1 \gg G$ but finite in an SNS-type model may be used to attain a KV-like model with non-Newtonian rheological behavior. When the strain rate is finite, the stiff non-equilibrium

response does not affect the total response of the material, but as the strain rate approaches zero (e.g., far from the bubble as $r \to \infty$), the stiff non-equilibrium response serves to regularize the diverging viscosity. Based on our tests, taking $G_1 = 1000G$ is sufficiently high to yield predictions of bubble dynamics that are independent of G_1, and when this idealization is made, the aforementioned six parameters reduces to a set of five parameters, $\{G, \alpha, K, m, \dot{\gamma}_0\}$. We refer to this model as the *non-Newtonian qKV model*.

2.3 Balance of linear momentum

The balance of linear momentum in the absence of external body forces requires that $\mathrm{div}\,\boldsymbol{\sigma} = \rho\mathbf{a}$, where $\mathrm{div}\,(\bullet)$ is the spatial divergence operator, $\rho = J^{-1}\rho_0$ is the spatial mass density, and $\mathbf{a}$ is the spatial description of the acceleration vector. Due to the idealization of spherical symmetry and the isotropy of the surrounding material, the only non-trivial component of the linear momentum balance equations is the radial component:

$$\frac{\partial \sigma_{rr}}{\partial r} + \frac{2}{r}\left(\sigma_{rr} - \sigma_{\theta\theta}\right) = \rho a_r, \tag{11}$$

where we have recognized that $\sigma_{\theta\theta} = \sigma_{\phi\phi}$ due to spherical symmetry.

At this stage, we note that the pressure associated with the Cauchy stress, $p = -(1/3)\mathrm{tr}\boldsymbol{\sigma}$, represents the "gauge" pressure–that is, the difference between the absolute pressure and the ambient atmospheric pressure p_∞. Then, the traction boundary conditions may be expressed in terms of the gauge pressures inside the bubble and in the far-field. The radial component of the traction boundary condition at the bubble wall ($r = R$) is

$$\sigma_{rr}|_{r=R} = -(p_\mathrm{b}(t) - p_\infty) + \frac{2\gamma}{R}, \tag{12}$$

where $p_\mathrm{b}(t)$ is the absolute pressure inside the bubble, $(p_\mathrm{b}(t) - p_\infty)$ is the gauge pressure inside the bubble, and γ is the surface tension of the bubble interface. The evolution of the time-dependent absolute pressure inside the bubble $p_\mathrm{b}(t)$ is governed by the physics of the bubble contents, which we assume to be a homobaric mixture of water vapor and non-condensible gas[21,41–43]. The mathematical description of bubble contents and resulting evolution equation for $p_\mathrm{b}(t)$ are described in detail in Estrada *et al.* [21] and briefly summarized in Appendix A.

In the far-field, the stress approaches a state of hydrostatic pressure: $\boldsymbol{\sigma}|_{r\to\infty} = -p_\mathrm{f}(t)\mathbf{1}$, where $p_\mathrm{f}(t)$ is the time-dependent, far-field gauge pressure, which is prescribed for a given problem. For example, as discussed in Section 3.3, in laser-induced cavitation, the far-field absolute pressure simply remains the ambient atmospheric pressure, so that the far-field gauge pressure is zero. In ultrasound-induced cavitation, $p_\mathrm{f}(t)$ is a time-varying, acoustic forcing[23,28,29]. Therefore, the far-field boundary condition for the radial stress component is

$$\sigma_{rr}|_{r\to\infty} = -p_\mathrm{f}(t). \tag{13}$$

3 Modeling of bubble dynamics

In this section, we describe two approaches for modeling the dynamics of spherical bubbles in soft viscoelastic media. The first is based on the Keller-Miksis (KM) equation[36], which reduces the balance of linear momentum partial differential equation (PDE) (11) to an ordinary differential equation (ODE) and enables an efficient computation of the bubble dynamics under the idealization of slight compressibility and for relatively simple constitutive descriptions of the surrounding material. In the second approach, the governing differential equation (11) is solved in the surrounding material using the finite-element method, which does not restrict the constitutive description of the surrounding material and allows for a higher fidelity description of the physics but is more computationally costly.

3.1 Keller-Miksis equation

The balance of linear momentum is reduced to an ODE by first assuming ideal incompressibility in the surrounding material ($J = 1$) and then integrating Eq. (11) over r from $r = R$ to $r \to \infty$ and applying the traction boundary conditions, Eqs. (12) and (13). The result is the Rayleigh-Plesset (RP) equation[34,35] governing the evolution of the bubble radius $R(t)$:

$$R\ddot{R} + \frac{3}{2}\dot{R}^2 = \frac{1}{\rho}\left(p_\mathrm{b} - p_\infty - p_\mathrm{f} - \frac{2\gamma}{R} + S\right), \tag{14}$$

where the stress integral S is given by

$$S = \int_R^\infty \frac{2}{r}\left(\sigma_{rr} - \sigma_{\theta\theta}\right) dr. \tag{15}$$

We note that, in Eq. (14), because ideal incompressibility has been assumed, the spatial mass density ρ is constant and equal to the referential mass density ρ_0.

However, the assumption of ideal incompressibility fails to account for energy transfer through radial acoustic emission from the bubble to the far field, which has a significant impact on the bubble dynamics. Keller and Miksis[36] extended the RP approach to account for slight compressibility of the surrounding material by incorporating the material's finite longitudinal wave speed c into the description of the far-field, resulting in the following modified evolution equation for the bubble radius $R(t)$:

$$\left(1 - \frac{\dot{R}}{c}\right)R\ddot{R} + \frac{3}{2}\left(1 - \frac{\dot{R}}{3c}\right)\dot{R}^2 = \frac{1}{\rho}\left(1 + \frac{\dot{R}}{c}\right)\left(p_\mathrm{b} - p_\infty - p_\mathrm{f} - \frac{2\gamma}{R} + S\right) + \frac{1}{\rho}\frac{R}{c}\dot{\left(p_\mathrm{b} - p_\mathrm{f} - \frac{2\gamma}{R} + S\right)}, \tag{16}$$

where the definition of the stress integral S given in Eq. (15) remains unchanged. The KM equation is accurate to first order in the ratio of the bubble wall velocity to the longitudinal wave speed in the surrounding material $\dot{R}/c$[44], i.e., the Mach number at the bubble wall. Note that in the limit of ideal incompressibility, $\dot{R}/c \to 0$, and the KM equation (16) reduces to the RP equation (14).

The constitutive behavior of the surrounding material enters both the RP and KM equations through the stress integral, Eq. (15). For certain constitutive models, the stress integral may be straightforwardly calculated analytically. For example, for the qKV model, in which the Cauchy stress is given by Eq. (6), under the assumption of ideal incompressibility ($J = 1$), the stress integral is[22]

$$S = \frac{(3\alpha-1)G}{2}\left[5-\left(\frac{R_0}{R}\right)^4-\frac{4R_0}{R}\right]-\frac{4\mu\dot{R}}{R} + 2\alpha G\left[\frac{27}{40}+\frac{1}{8}\left(\frac{R_0}{R}\right)^8+\frac{1}{5}\left(\frac{R_0}{R}\right)^5+\left(\frac{R_0}{R}\right)^2-\frac{2R}{R_0}\right]. \quad (17)$$

Note that when strain-stiffening is neglected ($\alpha = 0$), the stress integral reduces to that for the NH-KV model[30]. However, for more rheologically complex constitutive models, such as the SNS-type models of Section 2.2.2, closed-form, analytical expressions for the stress integral may not be obtainable, complicating the application of the KM equation.

In subsequent sections, to obtain numerical solutions for bubble dynamics using the KM equation when the surrounding material is described by a constitutive model possessing a closed-form stress integral, Eq. (16) is evolved forward in time in conjunction with the governing equations for the bubble contents (Appendix A) using a variable-step, variable-order solver (MATLAB `ode15s`).

3.2 Full-field solution using finite elements

The KM equation (16) is widely used to describe spherical bubble dynamics arising during inertial cavitation; however, as pointed out in Section 3.1, there are several limitations. First, it cannot account for moderate compressibility that can arise during more violent bubble collapse[22]. Second, calculation of the stress integral, Eq. (15), can be intractable for complex constitutive models. Therefore, while the KM equation provides an efficient route for predicting bubble dynamics in certain scenarios, these limitations motivate the need for a full-field description of the surrounding material, in which the dependence on the radial coordinate r is retained and not integrated out.

We maintain the assumption of spherical symmetry, and thus, the only differential equation under consideration is the radial component of the balance of linear momentum, Eq. (11), which we solve using the finite-element (FE) method. There are several practical matters that must be addressed to obtain FE solutions. First, in full-field calculations, the far-field must be truncated at a finite value of the radial coordinate. We denote the undeformed radius of the outer boundary after truncation as $R_{0,\infty}$ and its deformed counterpart as R_∞. Throughout, we take $R_{0,\infty} = 200R_0$, which we have verified to be sufficiently large so as to accurately approximate an infinite domain. Second, in full-field simulations, radial acoustic waves emitted from the bubble to the far field will reflect off of the outer boundary and refocus on the bubble, leading to incorrect numerical predictions. To mitigate this effect, a "quiet" boundary is implemented at the outer boundary[45], in which a normal traction of $\sigma_{rr}|_{r=R_\infty} = -\rho_0 c v_r|_{r=R_\infty}$ is applied at $r = R_\infty$. As a final point, in ultrasound-induced cavitation, it is impractical to apply the acoustic forcing $p_\mathrm{f}(t)$ at the outer boundary due to the presence of the quiet boundary. Moreover, such an approach would require simulating the additional time that it takes for the acoustic pulse to travel inward from the outer boundary to the bubble. Instead, in FE simulations of ultrasound-induced cavitation, the acoustic forcing is applied directly at the bubble wall, which makes direct comparisons of FE and KM simulations straightforward. As a result of these three adjustments to the problem definition, for FE simulations, the boundary conditions, Eqs. (12) and (13), are modified as follows:

$$\begin{cases}\sigma_{rr}|_{r=R} = -(p_\mathrm{b}(t) - p_\infty - p_\mathrm{f}(t)) + \dfrac{2\gamma}{R},\\ \sigma_{rr}|_{r=R_\infty} = -\rho_0 c v_r|_{r=R_\infty}.\end{cases} \quad (18)$$

Equations (11) and (18) represent the strong form of the balance of linear momentum. In order to recast the balance of linear momentum in a variational formulation, we introduce a scalar test field $\eta(r)$. The weak form is obtained by multiplying Eq. (11) by the test field, integrating over the domain, applying the divergence theorem, and using the boundary conditions, Eq. (18). The result is

$$-\int_R^{R_\infty}\left(\sigma_{rr}\frac{d\eta}{dr}+2\frac{\sigma_{\theta\theta}}{r}\eta\right)(4\pi r^2\,dr)-\rho_0 c(v_r\eta)|_{r=R_\infty}(4\pi R_\infty^2) + \left(p_\mathrm{b}-p_\infty-p_\mathrm{f}-\frac{2\gamma}{R}\right)\eta|_{r=R}(4\pi R^2) = \int_R^{R_\infty}\rho a_r\eta(4\pi r^2 dr). \quad (19)$$

Equation 19 is then used as the basis for a conventional explicit dynamic finite-element formulation. Briefly, the undeformed domain is spatially discretized using n_Elem equally-sized finite elements, which are each $(R_{0,\infty} - R_0)/n_\mathrm{Elem}$ in length. In this study, we use $n_\mathrm{Elem} = 1000$. We utilize one-dimensional, linear, two-noded finite elements, in which the radial displacement field u_r is interpolated inside each element using linear shape functions. A standard Galerkin approach is employed in that the test field is interpolated by the same shape functions. The resulting finite-element equations of motion are explicitly integrated in time using the explicit central difference scheme with a lumped mass matrix computed via the row-sum method. An adaptive time increment is employed, in which the time increment is chosen to be one third of the stable time increment calculated based on the smallest deformed element length, and the bubble pressure p_b is explicitly updated within each finite-element time increment by solving the governing equations for the physics of the bubble contents (Appendix A). We close this section by reiterating that the FE-based approach does not place restrictions on the constitutive model used to describe the surrounding material, and that we may straightforwardly incorporate any complex constitutive model for the surrounding material, including the SNS-type models of Section 2.2.2, into the cavitation modeling framework.

3.3 Initial conditions in laser-induced and ultrasound-induced cavitation bubbles

In this work, we consider both laser-induced cavitation (LIC) and ultrasound-induced cavitation (UIC). When simulating LIC, we initialize numerical simulations starting at the time that the bubble is at its maximum radius ($R = R_{\max}$). This is done because the initial growth phase of the bubble involves laser breakdown of the liquid and associated plasma physics, which is not accounted for in the cavitation modeling framework. When the bubble is at its maximum radius, we idealize the system as being in thermodynamic equilibrium with the surroundings, though not in mechanical equilibrium. The driving force for the subsequent cavitation dynamics is the gauge pressure inside the bubble modified by the Laplace pressure ($p_b - p_\infty - 2\gamma/R$), and in LIC, the far-field gauge pressure remains zero ($p_f = 0$). For KM-based numerical solutions, the bubble radius and velocity are initialized as $R(t=0) = R_{\max}$ and $\dot{R}(t=0) = 0$, respectively. For FE-based numerical simulations, the initial displacement field is prescribed based on the incompressible solution, i.e., $u_r(r_0, t=0) = (r_0^3 - R_0^3 + R_{\max}^3)^{1/3} - r_0$,† and the initial velocity field is zero everywhere, i.e., $\dot{u}_r(r_0, t=0) = 0$. For both approaches, the bubble contents are initialized as discussed in Appendix A.

Next, for UIC, we simulate the bubble dynamics from the initial growth phase through the first collapse and subsequent rebound cycles as the bubble approaches its undeformed radius. The bubble is initially in mechanical equilibrium with the surroundings. Therefore, for KM-based simulations, the initial conditions are $R(t=0) = R_0$ and $\dot{R}(t=0) = 0$, and for FE-based simulations, the initial conditions are $u_r(r_0, t=0) = \dot{u}_r(r_0, t=0) = 0$. The initial conditions for the bubble contents for both approaches are given in Appendix A. For UIC, the driving force for the bubble dynamics is the time-dependent far-field gauge pressure $p_f(t)$, which we take to be given in the following form:

$$p_f(t) = \begin{cases} p_A \left(\dfrac{1 + \cos[\omega(t-\delta)]}{2} \right)^n & \text{if } |t-\delta| \leq \dfrac{\pi}{\omega}, \\ 0 & \text{if } |t-\delta| > \dfrac{\pi}{\omega}. \end{cases} \tag{20}$$

This half-cycle waveform for the far-field gauge pressure is based on representative experimental acoustic pulses and has been extensively used in prior studies of UIC[5–7,23,28,29,46]. In this study, motivated by the experiments of Wilson *et al.*[28], the frequency $f = \omega/2\pi$ of the half-cycle pulse is taken to be 1 MHz. The time delay δ is simply $\delta = \pi/\omega$, so that the waveform begins at $t = 0$, and the dimensionless shape parameter n is chosen to be $n = 3.7$ as in prior studies to best represent experimental acoustic pulses. Finally, the peak tensile pressure $p_A < 0$ is varied in the simulations of the subsequent section in order to consider a range of consequent bubble amplitudes.

† Based on our tests, for the values of $R_{\max}$ and R_0 and the material parameters considered in this work, FE simulations using an initial condition based on the incompressible solution and an initial condition based on the compressible, equilibrium displacement field yield indistinguishable results for the bubble dynamics, so the incompressible displacement field is used for the initial condition for expedience.

Table 1 Parameters used in the studies of Sections 4 and 5

Parameter	Value	Parameter	Value
ρ_0	1060 kg/m^3	c	1430 m/s
p_∞	101.3 kPa	γ	5.6×10^{-2} N/m

4 Effect of material compressibility on bubble dynamics

In this section, we compare FE-based and KM-based simulations of bubble dynamics for both LIC and UIC. The purpose of this exercise is twofold: (1) to verify our FE-based simulation approach and (2) to establish a threshold for when the bubble dynamics involves material compressibility beyond that accounted for in the KM-based approach. Recall that the KM-based approach accounts only for slight far-field compressibility, while the FE-based approach accounts for compressibility in the full field, using an equation of state stemming from the term involving J in the free-energy density function, Eq. (3). In this section, we utilize the NH-KV model, so that solutions may be obtained using both approaches, and the quantitative values used for ρ_0, c, p_∞, and γ are summarized in Table 1.

To probe the role of material compressibility in bubble dynamics, we begin by considering LIC for several different values of $R_{\max}/R_0$, while keeping the material parameters of the NH-KV model, G and μ, fixed and equal to $G = 10$ kPa and $\mu = 0.03$ Pa·s. Figure 3(a) shows radius versus time curves in the case of LIC for $R_{\max}/R_0 = 2$, 4, and 7, where $R_0 = 22.5\,\mu$m. For LIC, the normalized radius is $R^* = R/R_{\max}$, and the normalized time is $t^* = (t/R_{\max})\sqrt{p_\infty/\rho_0}$. The FE-based calculations are presented as solid lines, and the KM-based calculations are presented as dashed lines. For each case, we define the maximum Mach number as $\max_t(\dot{R}(t))/c$, where c is the longitudinal wave speed in the surrounding material. We can see that for the case of $R_{\max}/R_0 = 2$, for which the maximum Mach number is on the order of 0.01 and bubble collapse is the least violent, the two approaches yield nearly identical results, verifying the FE-based simulation approach. As $R_{\max}/R_0$ increases, bubble collapse becomes more violent with an increasing maximum Mach number, and the two approaches begin to give rise to increasingly different results, indicating that material compressibility not accounted for in the KM-approach becomes more important for more violent bubble collapse.

As an alternate approach to probing the role of material compressibility, we consider LIC for three different values of the viscosity, $\mu = 0.003, 0.032$, and 0.1 Pa·s, for a fixed radius ratio of $R_{\max}/R_0 = 4$, while maintaining $G = 10$ kPa and $R_0 = 22.5\,\mu$m. Figure 3(b) shows the corresponding radius versus time curves, calculated using both FE-based and KM-based simulations. For the highest value of the viscosity, the bubble dynamics are more damped and less violent with a maximum Mach number of approximately 0.03. Consequently, the two approaches give similar results. As the viscosity is decreased, the maximum Mach number increases, bubble collapse becomes more violent, and the discrepancy between the two approaches grows. In general, for violent collapse, the compressibility of the surrounding material is more

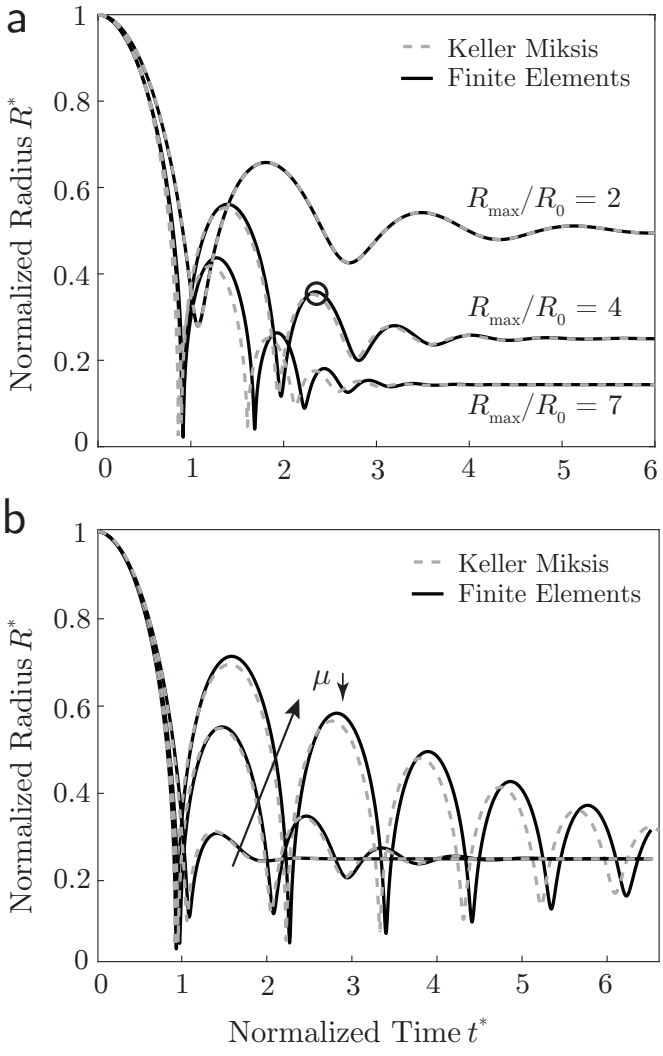

Fig. 3 Effect of (a) the radius ratio R_{max}/R_0 and (b) the viscosity of the surrounding material μ on normalized radius versus time curves for LIC. FE-based simulations are shown as solid lines, and KM-based simulations are shown as dashed lines. The open circle in (a) illustrates the time t_c used in Eq. (21) to calculate ΔR_{RMS}.

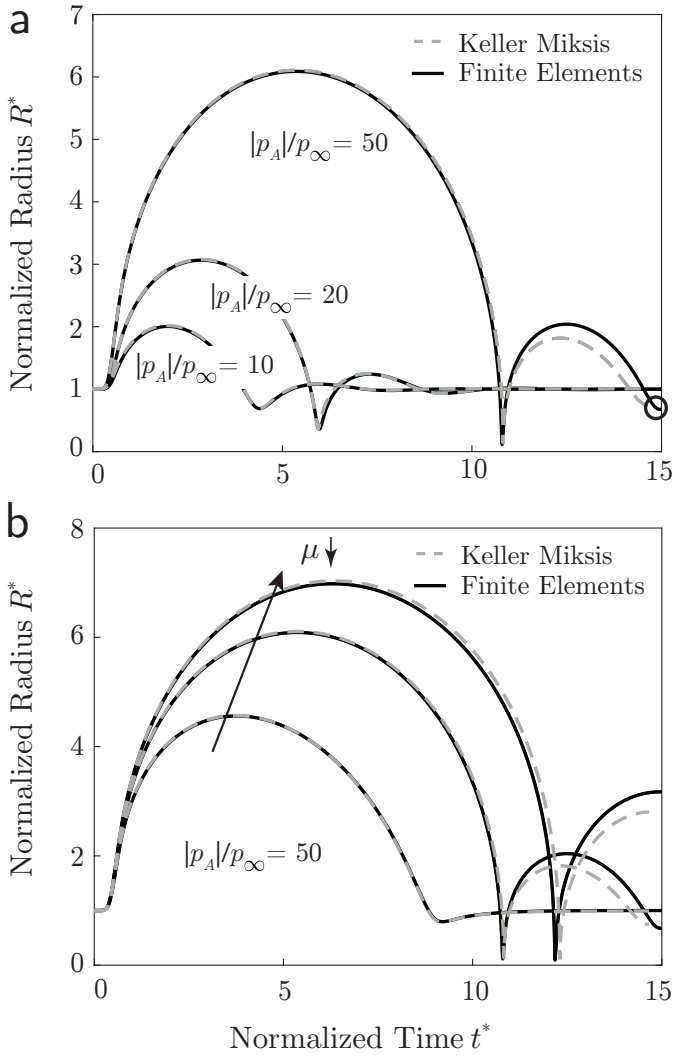

Fig. 4 Effect of (a) the peak tensile pressure $|p_A|/p_\infty$ and (b) the viscosity of the surrounding material μ on normalized radius versus time curves for UIC. FE-based simulations are shown as solid lines, and KM-based simulations are shown as dashed lines. The open circle in (a) illustrates the time t_c used in Eq. (21) to calculate ΔR_{RMS}.

important, giving rise to the discrepancy between the two approaches.

Similar observations are made for the case of UIC. Figure 4(a) shows normalized radius versus time curves for UIC for peak tensile pressures of $|p_A|/p_\infty = 10, 20$, and 50, where $G = 10$ kPa, $\mu = 0.03$ Pa·s, and $R_0 = 10\,\mu$m. For UIC, the normalized radius is $R^* = R/R_0$, and the normalized time is $t^* = (t/R_0)\sqrt{p_\infty/\rho_0}$. As the peak tensile pressure increases, the cavitation amplitude increases, larger radius ratios (R_{max}/R_0) are attained, and the consequent collapse is more violent with a greater maximum Mach number. As for LIC, as the radius ratio increases, the discrepancy between the FE-based and KM-based simulations grows. Figure 4(b) shows normalized radius versus time curves for three different values of the viscosity, $\mu = 0.003, 0.032$, and 0.1 Pa·s, for a fixed peak tensile pressure of $|p_A|/p_\infty = 50$, while maintaining $G = 10$ kPa and $R_0 = 10\,\mu$m. Again, as the viscosity decreases, larger radius ratios are attained, the bubble collapse becomes more violent, and there is an increase in the discrepancy between the two simulation approaches.

To quantify the discrepancy between FE-based and KM-based simulations and how it depends on the maximum Mach number, we utilize the root-mean-square of the difference between the normalized radius history calculated using FE-based and KM-based approaches:

$$\Delta R_{RMS} = \sqrt{\frac{1}{t_c}\int_0^{t_c} \left(R^*_{FE}(t^*) - R^*_{KM}(t^*)\right)^2 dt^*}, \qquad (21)$$

where $R^*_{FE}(t^*)$ and $R^*_{KM}(t^*)$ are the FE-calculated and KM-calculated normalized radius histories, and t_c is a characteristic normalized time for each case that corresponds to the second rebound time in LIC and the second collapse time in UIC (illustrated with open circle markers in Figs. 3(a) and 4(a), respectively). Further, for each case, we calculate the maximum Mach

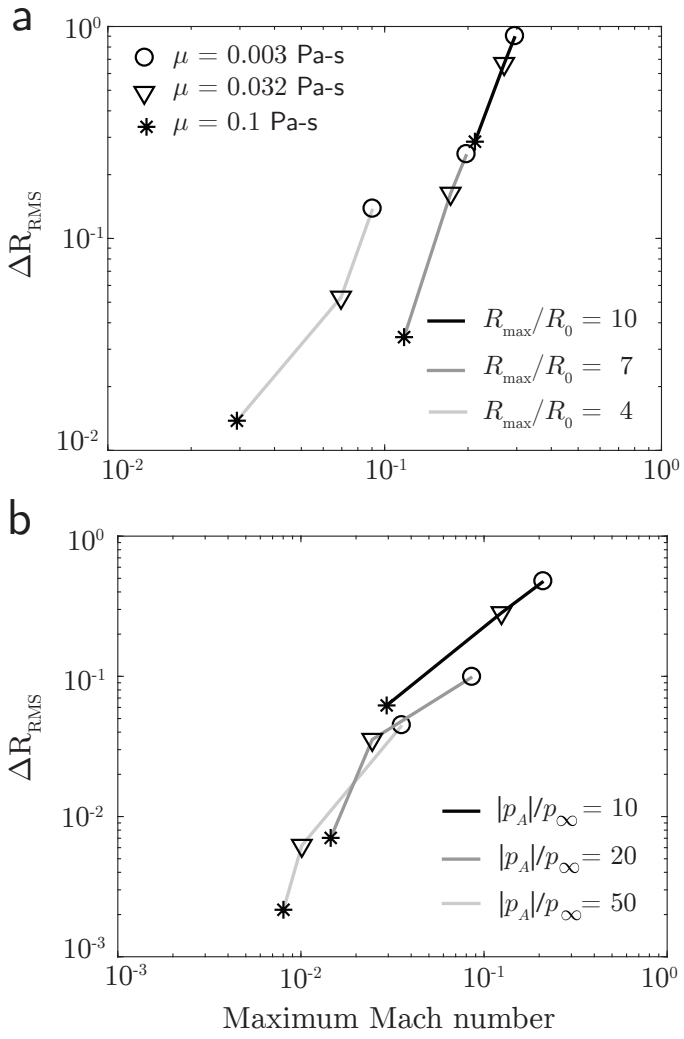

Fig. 5 Plots of ΔR_{RMS} versus the maximum Mach number for (a) LIC and (b) UIC. We observe that the discrepancy between the FE-based and KM-based simulations increases as the maximum Mach number increases across all cases considered.

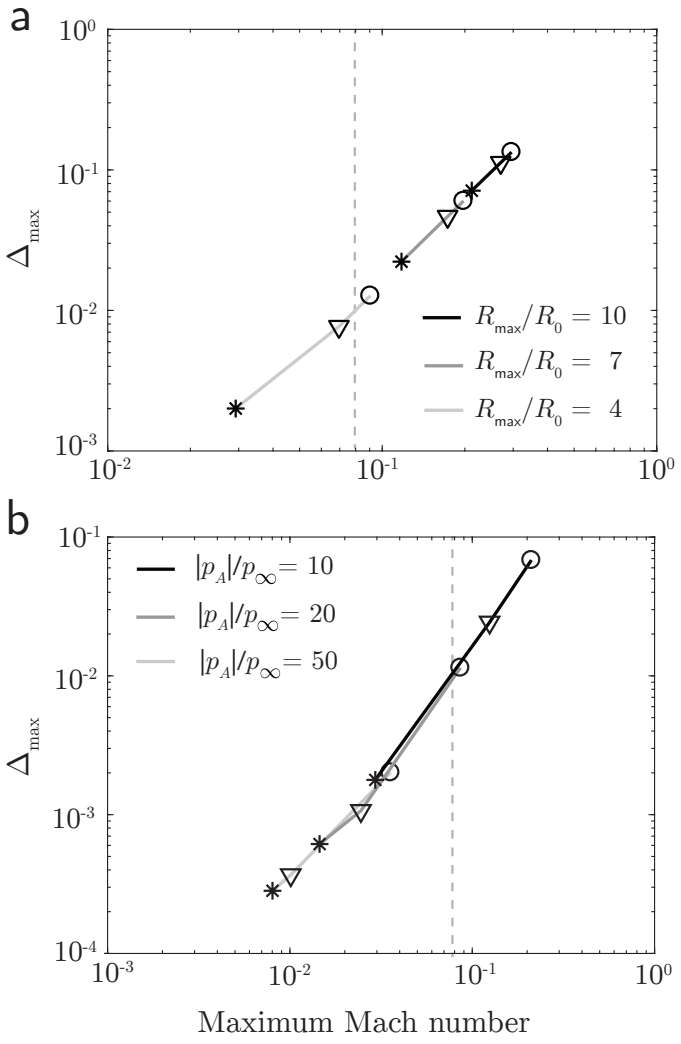

Fig. 6 Plots of Δ_{max} versus the maximum Mach number for (a) LIC and (b) UIC. The viscosity is denoted by the symbol type shown in the legend of Fig. 5(a). We observe that the maximum volumetric strain magnitude Δ_{max} increases as the maximum Mach number increases across all cases considered. In both LIC and UIC, for maximum Mach numbers less than about 0.08 (vertical dashed gray lines), Δ_{max} remains below 0.01.

number, $\max_t(\dot{R}(t))/c$. Figures 5(a) and (b) then show plots of ΔR_{RMS} versus the maximum Mach number for LIC and UIC, respectively. In Fig. 5(a), nine different combinations of radius ratio R_{max}/R_0 and viscosity μ are included for LIC, each represented by a symbol, where the viscosity is denoted by the symbol type, and the radius ratio is denoted by the shading of the connecting lines. As observed in Fig. 3, as the radius ratio R_{max}/R_0 increases or as the viscosity μ decreases, the maximum Mach number increases, indicating that bubble collapse becomes more violent. As a result, the discrepancy between FE-based and KM-based calculations, quantified by ΔR_{RMS}, increases by nearly two orders of magnitude over the range of maximum Mach numbers considered here. Similarly, in Fig. 5(b), nine different combinations of peak tensile pressure $|p_{\mathrm{A}}|/p_\infty$ and viscosity μ are included for UIC and denoted in the same manner as in Fig. 5(a). Again, we observe that as the peak tensile pressure $|p_{\mathrm{A}}|/p_\infty$ increases or as the viscosity μ decreases, bubble collapse becomes more violent, and the maximum Mach number and ΔR_{RMS} both increase.

For both LIC and UIC, a rough collapse in ΔR_{RMS} versus maximum Mach number is observed across the cases considered. We have confirmed that both FE-based and KM-based simulations are sufficiently refined both temporally and spatially, so that the discrepancy ΔR_{RMS} is attributable to the different approaches used to account for material compressibility in the two methods.

The results of Fig. 5 suggest that the increasing maximum Mach number associated with violent bubble collapse is accompanied by increased compressibility in the surrounding material. To make this connection more concrete, we consider the volumetric strain field $\Delta = \ln J$, calculated using the FE approach. The maximum volumetric strain magnitude in the surroundings occurs at the bubble wall $r = R$ at first collapse in all cases of both LIC and UIC considered in this section. We define the maximum volumetric strain magnitude as $\Delta_{\mathrm{max}} = \max_t(|\Delta(r = R, t)|)$. Figures 6(a) and (b) then show plots of Δ_{max} versus the maximum Mach

number for LIC and UIC, respectively, calculated using the FE approach. As in Fig. 5, the viscosity for each case is denoted by the symbol type, and the radius ratio in Fig. 6(a) and the peak tensile pressure in Fig. 6(b) are denoted by the shading of the connecting lines. For both LIC and UIC, a collapse is observed across the cases considered with maximum volumetric strain increasing as bubble collapse becomes more violent. Compressibility may be regarded as slight when the maximum volumetric strain remains on the order of 0.01 or less. Based on Fig. 6, for maximum Mach numbers less than about 0.08 (denoted by the vertical dashed gray lines), $\Delta_{\max}$ remains below 0.01, and material compressibility is slight. Correspondingly, the discrepancy between FE-based and KM-based simulations is minimal. But for maximum Mach numbers greater than about 0.08, $\Delta_{\max}$ is greater than 0.01, and material compressibility plays an increasingly significant role in the bubble dynamics. Consequently, ΔR_{RMS} grows, and FE-based simulations become more accurate, due to a higher fidelity description of the physics of material compressibility. These observations suggest a maximum Mach number of 0.08 may be used as a threshold for when bubble dynamics involves material compressibility beyond that accounted for in the KM-based approach. We note that this threshold complements the experimental observations of Yang *et al.* [22] for polyacrylamide gel, who reported a transition from viscoelastic material behavior to more complex behavior at a maximum Mach number of 0.08, based on measurements of the radial positions of tracked material points in the surrounding material.

5 Characterizing the high-strain-rate behavior of polyacrylamide gels

Next, we utilize FE-based simulations in Inertial Microcavitation Rheometry (IMR) to obtain improved high-strain-rate properties for soft materials–a process that we refer to as FE-IMR. First, in Section 5.1, we revisit the experimental LIC data of Yang *et al.* [22] for violent bubble collapse in a stiff polyacrylamide gel and apply FE-IMR that accounts for material compressibility to obtain higher fidelity properties. Then, in Section 5.2, we consider the experimental data of Buyukozturk *et al.* [27] for particle-assisted LIC in a soft polyacrylamide gel over a range of cavitation amplitudes and use FE-IMR to characterize the high-strain-rate behavior, including non-Newtonian rheological behavior.

5.1 Stiff polyacrylamide gel

First, we consider the LIC experiments of Yang *et al.* [22] on polyacrylamide (PA) gels and focus on their "stiff" PA gel with a ground-state shear modulus of $G = 2.77$ kPa, determined through quasi-static testing. Ten LIC experiments were carried out on the stiff PA gel, yielding mean maximum and equilibrium radii of $330.26 \pm 30.36\,\mu$m and $46.52 \pm 4.28\,\mu$m, respectively, corresponding to a radius ratio of $R_{\max}/R_0 = 7.1$. The normalized radius $R^* = R/R_{\max}$ versus normalized time $t^* = (t/R_{\max})\sqrt{p_\infty/\rho_0}$ history for a representative LIC experiment in stiff PA gel from Yang *et al.* [22] is shown in Fig. 7 as square symbols. Throughout Section 5, following Estrada *et al.* [21], we use the values of ρ_0, c, p_∞, and γ summarized in Table 1.

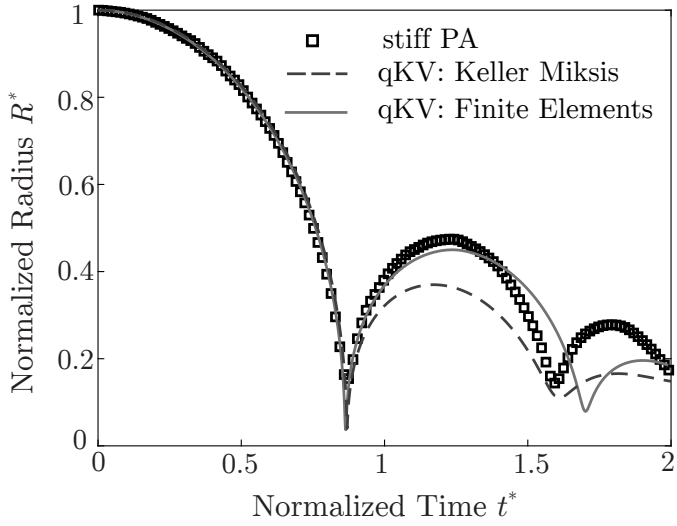

Fig. 7 Comparison of experimental data (symbols), numerical KM-IMR results (dashed line), and numerical FE-IMR results (solid line) for the normalized radius versus time history for stiff PA gel. For KM-IMR, only the first collapse was used to obtain best-fit material parameters, while FE-IMR utilizes the bubble radius history through the third collapse ($0 < t^* \lesssim 2$). Both approaches use the qKV model, and FE-IMR gives $\alpha = 0.48$ and $\mu = 0.158$ Pa·s as the best-fit material parameters, while KM-IMR gives $\alpha = 0.48$ and $\mu = 0.186$ Pa·s.

In applying KM-based IMR (KM-IMR) to LIC data for stiff PA, Yang *et al.* [22] made two key observations. First, Yang *et al.* [22] showed that KM-IMR cannot provide an adequate description of the physics beyond the first collapse for violently collapsing bubbles, which are marked by a maximum Mach number of greater than 0.08. This was experimentally observed in their work based on measurements of the kinematics of tracked material points in the surrounding material, and the results of Section 3.1 in the present work establish that compressibility begins to matter beyond this point, and that KM-IMR does not adequately account for compressibility beyond a maximum Mach number of 0.08. Thus, only the first collapse in the normalized radius versus time history was utilized in Yang *et al.* [22] to obtain best-fit material parameters for PA gels. Second, Yang *et al.* [22] concluded that for sufficiently large radius ratios, accounting for strain stiffening effects is crucial to improve the quality of the fitted material parameters for PA gels. Therefore, the quadratic Kelvin-Voigt (qKV) model, which accounts for strain stiffening, was utilized, and a strain-stiffening parameter of $\alpha = 0.48$ and a viscosity of $\mu = 0.186$ Pa·s were obtained based on least-squares data fitting, while maintaining the ground-state shear modulus to be equal to the quasi-static value of $G = 2.77$ kPa. The corresponding normalized radius versus time curve, fitted to the first collapse, is included in Fig. 7 as a dashed line.

Since FE-IMR accounts for material compressibility, this approach may be utilized to obtain higher fidelity estimates of high-strain-rate material properties from normalized radius versus time data for violently-collapsing LIC bubbles beyond first collapse. Here, we revisit the LIC experiments of Yang *et al.* [22] on stiff PA gel and apply FE-IMR. We broaden the portion of the normalized radius versus time history used for fitting beyond the first

collapse to include the history through the third collapse ($t^* \lesssim 2$ in Fig. 7). Moreover, we consider a more general constitutive model and utilize the non-Newtonian qKV model. As discussed in Section 2.2.2, the non-Newtonian qKV model is obtained from an SNS-type constitutive modeling approach, in which the non-equilibrium shear modulus G_1 is taken to be much greater than the ground-state shear modulus G. Here we take $G_1 = 1000G$. As in Yang *et al.* [22], we take the equilibrium shear modulus to be its quasi-static value $G = 2.77$ kPa, and the bulk modulus is given through the longitudinal wave speed by $K = \rho_0 c^2 - (4/3)G$, leaving three adjustable material parameters: the strain-stiffening parameter α, the strain-rate sensitivity exponent m, and the reference strain rate $\dot{\gamma}_0$. We then perform least-squares fitting between experimental radius versus time curves for stiff PA gel and curves computationally obtained using FE-IMR with the adjustable parameters $\{\alpha, m, \dot{\gamma}_0\}$. As a result of this procedure, we find that the best-fit value of the rate-sensitivity exponent m is one, meaning that the rheological behavior of the stiff PA gel is Newtonian. Recalling that for the Newtonian case, the constant shear viscosity is $\mu = G/\dot{\gamma}_0$, the best-fit parameters determined using FE-IMR are $\alpha = 0.48$ and $\mu = 0.158$ Pa·s. The corresponding normalized radius versus time curve is included in Fig. 7 as a solid line.

Comparing the fitted bubble radius histories for FE-IMR and KM-IMR in Fig. 7, we observe that both FE-IMR and KM-IMR capture the first collapse very well. However, beyond the first collapse, KM-IMR underestimates the height of the second rebound, while FE-IMR manages to capture it well. Although there is some time delay in the second collapse predicted by FE-IMR, overall, it captures the bubbles dynamics in stiff PA gel well, yielding a more precise estimation of the material parameters. Comparing the material parameters determined using FE-IMR and KM-IMR, we note that the value of the fitted strain-stiffening parameter α does not change, while the value of the fitted viscosity decreases from 0.186 Pa·s to 0.158 Pa·s. This may be understood as follows. As observed in Fig. 3(a), KM-based simulations predict that first collapse occurs slightly faster than corresponding FE-based simulations, due to the differences in how the two methods account for material compressibility. To compensate for this, when fitting the experimental bubble dynamics during first collapse, KM-IMR overestimates the viscosity, slowing down the predicted collapse dynamics to be in line with the experimental data but leading to the subsequent rebounds being overdamped. The ability of FE-IMR to more precisely capture the second rebound stems from the fact that FE-IMR accounts for the compressibility of the surrounding material, which slightly delays the collapse time as shown in Section 4. Thus, we conclude that accounting for material compressibility is important when dealing with violently collapsing bubbles, and doing so leads to higher fidelity estimates of material properties–in particular, the viscosity–of soft materials when applying IMR to experimental data.

5.2 Soft polyacrylamide gel

Next, we consider the LIC experiments of Buyukozturk *et al.* [27] for a "soft" PA gel with a ground-state shear modulus of $G = 461 \pm 4$ Pa.‡ In Buyukozturk *et al.* [27], three types of micron-sized nucleation seed particles (glass, stainless steel, and paramagnetic-coated polyethylene beads) were dilutely dispersed in the soft PA gel. Scanning Electron Microscope (SEM) images of glass and paramagnetic-coated polyethylene seed particles are reproduced from Buyukozturk *et al.* [27] in Fig. 8(a). In each LIC experiment, the laser pulse was focused on a single seed particle, and varying laser energies were utilized across different experiments to achieve a range of radius ratios ($4 \lesssim R_{\max}/R_0 \lesssim 9$). LIC experiments without seed particles were also carried out. Schematics of the cavitation focal point in the gel specimen both without and with seed particles are included in Fig. 8(a). The normalized radius $R^* = R/R_{\max}$ versus normalized time $t^* = (t/R_{\max})\sqrt{p_\infty/\rho_0}$ histories for representative LIC experiments from Buyukozturk *et al.* [27] in soft PA gel using paramagnetic-coated polyethylene seed particles, glass seed particles, and no seed particles are shown in Figs. 8(b), (c), and (d), respectively, as square symbols. All three of the representative cases correspond to a nominal laser energy of 117.8 μJ. The resultant maximum bubble radii for the representative cases were $R_{\max} = 271.63$, 239.14, and 199.21 μm for paramagnetic-coated polyethylene seed particles, glass seed particles, and no seed particles, respectively, and the corresponding equilibrium radii were $R_0 = 56.28$, 41.19, and 23.26 μm, corresponding to radius ratios of $R_{\max}/R_0 = 4.8$, 5.8, and 8.6. Thus, through the use of seed particles, different deformation amplitudes and rates were achieved in the same material, and the aim of this section is to apply FE-IMR to collectively fit the experimental data of Fig. 8 and extract a set of material parameters for soft PA gel at high strain rates.

To apply FE-IMR, we begin with the Newtonian version of the qKV model discussed in Section 2.2.2 and used for the stiff PA gel in Section 5.1. We take the equilibrium shear modulus to be the quasi-static value of $G = 461$ Pa, leaving two adjustable parameters: the strain-stiffening parameter α and the shear viscosity μ. For fitting, we utilize the three normalized radius versus time histories in Fig. 8, each through their respective third collapse point: $t^* \lesssim 3.0$ in Fig. 8(b), $t^* \lesssim 2.7$ in Fig. 8(c), and $t^* \lesssim 2.1$ in Fig. 8(d). Then, we perform least-squares fitting between the three experimental histories and the corresponding histories calculated using FE-IMR with one set of adjustable parameters $\{\alpha, \mu\}$. We find that the best-fit parameters for the qKV model determined using FE-IMR are $\alpha = 0.75$ and $\mu = 0.0646$ Pa·s. We note that these values are comparable to the best-fit values determined in Buyukozturk *et al.* [27] using KM-IMR with the qKV model (see Fig. 6(c) of Buyukozturk *et al.* [27]). The best-fit normalized radius versus time curves for the qKV model are included in Figs. 8(b)-(d) as dashed lines. Overall, the fit is reasonable, especially for first collapse in all cases and across the full history for the case of paramagnetic-coated polyethylene seed particles in Fig. 8(b), for which the radius ratio $R_{\max}/R = 4.8$ is the smallest of the cases considered. For the largest radius ratio of $R_{\max}/R = 8.6$ corresponding to the case of no seed particles in Fig. 8(d), the best-fit predictions of the qKV

‡ We note that this is a slightly different PA gel than the soft PA gel considered in Yang *et al.* [22], which had a ground-state shear modulus of $G = 570$ Pa.

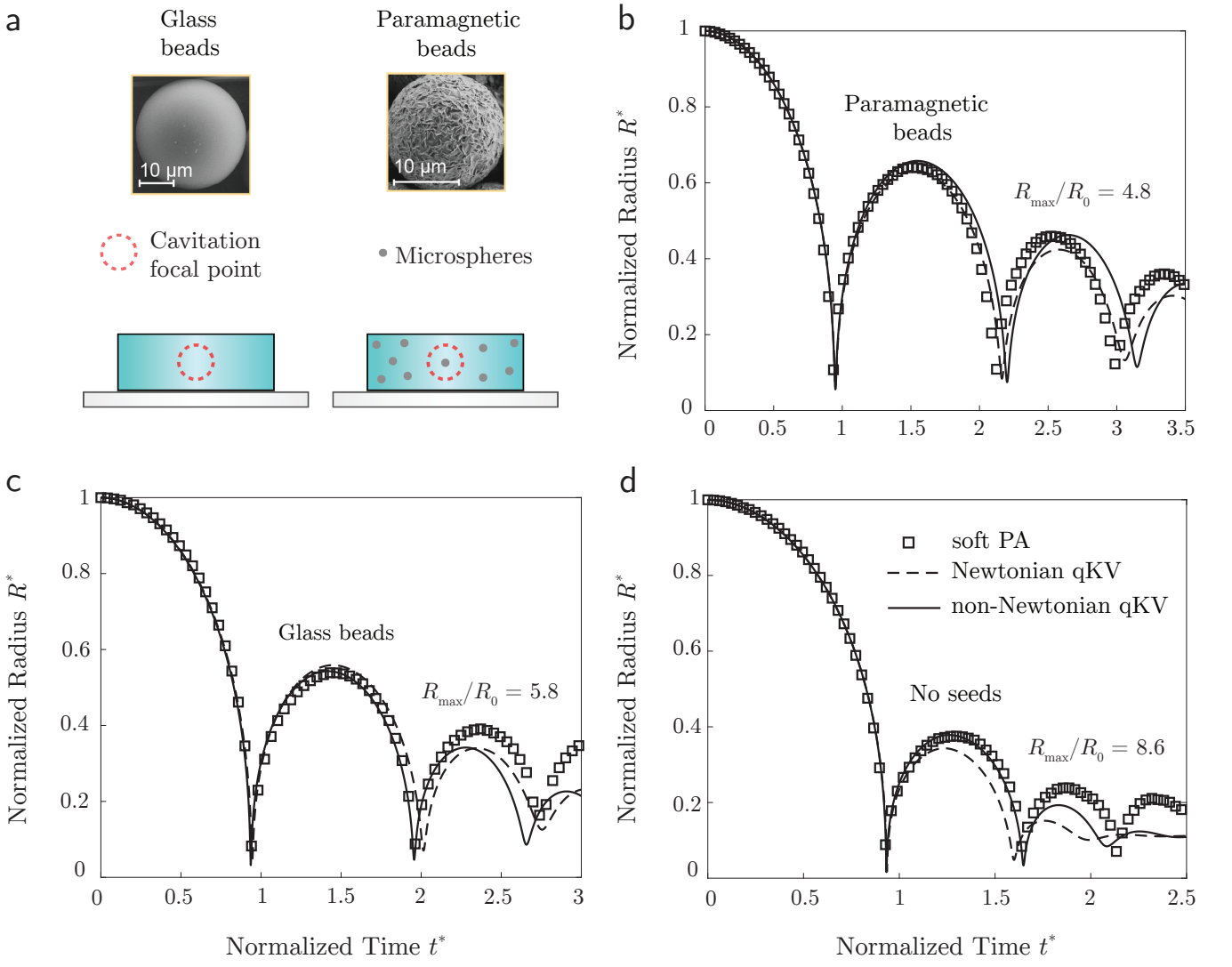

Fig. 8 Application of FE-IMR to soft PA gel. (a) SEM images of glass and paramagnetic-coated polyethylene seed particles from Buyukozturk *et al.* [27] and schematics of the cavitation focal point both without and with seed particles. (b-d) Comparison of experimental data (symbols), numerical FE-IMR results using the Newtonian qKV model (dashed lines), and numerical FE-IMR results using the non-Newtonian model (solid lines) for normalized radius versus time histories for soft PA gel. Different radius ratios were achieved in Buyukozturk *et al.* [27] using (b) paramagnetic-coated polyethylene seed particles ($R_{\max}/R_0 = 4.8$), (c) glass seed particles ($R_{\max}/R_0 = 5.8$), and (d) no seed particles ($R_{\max}/R_0 = 8.6$). The best-fit material parameters for the Newtonian qKV model were $\alpha = 0.75$ and $\mu = 0.0646$ Pa·s, and the best-fit material parameters for the non-Newtonian qKV model were $\alpha = 0.75$, $\dot{\gamma}_0 = 6046\,\mathrm{s}^{-1}$ and $m = 0.9$.

model are overdamped for the second and third collapses.

Next, to obtain refined high-strain-rate properties for the soft PA gel, we apply FE-IMR using the non-Newtonian qKV model and follow a similar fitting procedure as described in the preceding paragraph. Recall that the non-Newtonian qKV model stems from an SNS-type constitutive modeling approach, and as in Section 5.1, we continue to take the non-equilibrium shear modulus to be $G_1 = 1000G$. Then, we take the equilibrium shear modulus to be the quasi-static value of $G = 461$ Pa, leaving three adjustable parameters: $\{\alpha, m, \dot{\gamma}_0\}$. Again, we perform collective least-squares fitting of FE calculations to the experimental histories of Figs. 8(b)-(d) through the third collapse. The resulting best estimates of the material parameters of the non-Newtonian qKV model are $\alpha = 0.75$, $\dot{\gamma}_0 = 6046\,\mathrm{s}^{-1}$ and $m = 0.9$, and the corresponding best-fit normalized radius versus time curves are included as solid lines in Figs. 8(b)-(d). The value of the stiffening parameter α is the same as the value determined for the Newtonian qKV model, while a best-fit value of the rate-sensitivity exponent of $m = 0.9$ is determined. Therefore, the primary difference between predictions of the Newtonian and non-Newtonian versions of the qKV model is the shear-thinning rheological behavior accounted for in the non-Newtonian version. We observe that the overall quality of the fitting is improved in Fig. 8. The first collapse as well as the following rebound and second collapse are captured across all three radius ratios. Therefore, by incorporating non-Newtonian, shear-thinning rheological behavior in the constitutive description of the surrounding material, an improved set of high-strain-rate material parameters may be determined.

6 Concluding remarks

In this work, we have developed a finite-element-based approach for modeling the cavitation dynamics of spherical bubbles in soft viscoelastic media, which may be applied to both laser-induced and ultrasound-induced cavitation. Compared to the standard approach that utilizes the Keller-Miksis equation[21–23,25], the FE-based approach can account for more complex constitutive behavior of the surrounding material. In this work, we focused on two aspects of the behavior of the surrounding material: compressibility and non-Newtonian rheological behavior. Regarding material compressibility, we observed that for both LIC and UIC, the discrepancy between FE-based and KM-based simulations grows with the maximum Mach number, and that for maximum Mach numbers greater than about 0.08, the bubble dynamics involves material compressibility beyond that accounted for in the KM-based approach. Therefore, under this condition, FE-IMR may be used to obtain higher fidelity estimates of material properties. This was demonstrated by revisiting the LIC data of Yang *et al.* [22] for a stiff PA gel and applying FE-IMR to the normalized radius versus time history beyond first collapse to obtain a refined estimate of the material parameters of the qKV model. Regarding rheological behavior, we incorporated a non-Newtonian, power-law version of the qKV model into the FE-IMR framework and applied the model to the particle-assisted LIC data of Buyukozturk *et al.* [27] for a soft PA gel over a range of cavitation amplitudes to obtain a set of material parameters for soft PA gel at high strain rates. The trade-off of the FE-based approach compared to the KM-based approach is the additional computational expense required to solve the balance of linear momentum differential equation in the surrounding material. Therefore, FE-IMR is complementary to KM-IMR, since KM-IMR may be used to efficiently estimate material properties using simple models, which may be further refined using FE-IMR. The FE-based and KM-based codes used in this work have been made available to the community via GitHub (https://github.com/HenannResearchGroup).

Our modeling framework accounts for the dynamics of a single spherical bubble, which places limitations on when FE-IMR and KM-IMR may be applied. First, dynamic cavitation in soft viscoelastic materials can lead to complex, non-spherical instability patterns, including bubble surface wrinkles and creases as shown by Yang *et al.* [25,47]. Second, cavitation in anisotropic soft materials is expected to lead to non-spherical bubble shapes. Accounting for the effects of non-spherical bubble dynamics is beyond the capacity of spherical bubble modeling and requires full, three-dimensional modeling of the bubble dynamics, which is an important avenue for future work. Therefore, both FE-IMR and KM-IMR may only be applied to experimental $R(t)$ data in isotropic materials under situations in which the bubble remains spherically symmetric during the cavitation event in order to accurately estimate material parameters.

Beyond developing a three-dimensional framework for modeling non-spherical bubble dynamics, there remain several directions for future research work within the realm of spherical bubble modeling. First, we expect that FE-IMR may be used to study a broad selection of soft materials beyond PA gel, such as agarose and gelatin gels as well as biological tissues, and it remains to apply FE-IMR to these materials to extract high-strain-rate material properties. Second, since the FE-based approach does not place restrictions on the constitutive model used to described the surrounding material, additional material physics, such as damage and plasticity, may be considered. For example, past studies that incorporate damage models into a RP-based framework[32,48] have only considered simple damage models, due to the mathematical restrictions involved in evaluating the stress integral, Eq. (15). Thus, future work that implements continuum damage mechanics models into FE-IMR may be used to more accurately model the evolution of damage during inertial microcavitation. Finally, the current cavitation modeling framework employs the "cold medium" assumption, which idealizes the surrounding material as isothermal. Several previous works account for temperature evolution in the surroundings[29,43,49], and FE-IMR may be straightforwardly extended to solve the balance of energy equation for the evolution of the temperature field in the surroundings and potentially further refine the estimation of material parameters.

Conflicts of interest

There are no conflicts to declare.

Acknowledgments

This work was supported by funds from the Office of Naval Research under grants N00014-18-1-2625, N00014-21-1-2109, and N00014-22-1-2094 (under Dr. Timothy Bentley). Part of this research was conducted using computational resources at the Center for Computation and Visualization (CCV) at Brown University.

A Bubble contents

In this appendix, we summarize the equations governing the physics of the bubble contents. The modeling approach follows the literature on the physics of laser-induced cavitation bubbles[21,41–43], and a more detailed discussion may be found in Estrada *et al.* [21]. We idealize the bubble contents as a homobaric, two-phase mixture consisting of water vapor and non-condensible gas, which are both modeled as ideal gases. The (dimensionless) vapor mass fraction field $k(r,t)$ and the temperature field $T(r,t)$ inside the bubble ($0 \le r \le R$) evolve according to

$$\frac{\partial k}{\partial t} + v_{\mathrm{m}} \frac{\partial k}{\partial r} = \frac{1}{\rho_{\mathrm{m}} r^2} \frac{\partial}{\partial r} \left(\rho_{\mathrm{m}} r^2 D \frac{\partial k}{\partial r} \right) \tag{22}$$

and

$$\frac{\kappa}{\kappa - 1} \frac{p_{\mathrm{b}}}{T} \left(\frac{\partial T}{\partial t} + v_{\mathrm{m}} \frac{\partial T}{\partial r} \right) = \dot{p}_{\mathrm{b}} + \frac{1}{r^2} \frac{\partial}{\partial r} \left(r^2 K \frac{\partial T}{\partial r} \right) + \frac{\kappa}{\kappa - 1} \frac{p_{\mathrm{b}}}{T} \frac{\mathcal{R}_{\mathrm{v}} - \mathcal{R}_{\mathrm{g}}}{\mathcal{R}} D \frac{\partial k}{\partial r} \frac{\partial T}{\partial r}, \tag{23}$$

respectively, where

$$v_{\mathrm{m}}(r,t) = \frac{1}{\kappa p_{\mathrm{b}}} \left[(\kappa - 1) K \frac{\partial T}{\partial r} - \frac{1}{3} r \dot{p}_{\mathrm{b}} \right] + \frac{\mathcal{R}_{\mathrm{v}} - \mathcal{R}_{\mathrm{g}}}{\mathcal{R}} D \frac{\partial k}{\partial r} \tag{24}$$

Table 2 Parameters describing the physics of the bubble contents

Parameter	Value	Parameter	Value
D	24.2×10^{-6} m^2/s	κ	1.4
$\mathcal{R}_v$	0.462 kJ/kg·K	$\mathcal{R}_g$	0.287 kJ/kg·K
A	5.3×10^{-5} W/m·K^2	B	1.17×10^{-2} W/m·K
p_{ref}	1.17×10^{8} kPa	T_{ref}	5200 K
T_∞	298.15 K		

is the mixture velocity field, $\rho_m = p_b/\mathcal{R}T$ is the mixture density field, $\mathcal{R} = k\mathcal{R}_v + (1-k)\mathcal{R}_g$ is the mixture gas constant field, and $K(T) = AT + B$ is the temperature-dependent thermal conductivity of the mixture[50]. Finally, the ODE governing the evolution of the absolute pressure inside the bubble $p_b(t)$ is

$$\dot{p}_b = \frac{3}{R}\left[-\kappa p_b\dot{R} + (\kappa-1)K(T|_{r=R})\left.\frac{\partial T}{\partial r}\right|_{r=R} + \kappa p_b\frac{\mathcal{R}_v}{\mathcal{R}(k|_{r=R})}\frac{D}{1-k|_{r=R}}\left.\frac{\partial k}{\partial r}\right|_{r=R}\right]. \quad (25)$$

The constant parameters associated with the bubble contents are the binary diffusion coefficient D, the specific heats ratio of the mixture κ, the gas constants of the water vapor and non-condensible gas, $\mathcal{R}_v$ and $\mathcal{R}_g$, and the empirical constants describing the temperature-dependence of the thermal conductivity of the mixture, A and B, which are summarized in Table 2.

The boundary conditions for the PDEs governing the temperature field, Eq. (23), and the vapor mass fraction field, Eq. (22), at the bubble center ($r = 0$) are $\partial T/\partial r|_{r=0} = \partial k/\partial r|_{r=0} = 0$. It is assumed that the surrounding material remains isothermal at an ambient temperature of T_∞ (i.e., the "cold medium" assumption), so that the temperature boundary condition at the bubble wall is $T|_{r=R} = T_\infty$. Further, at the bubble wall, the partial pressure of the water vapor is taken to be equal to its saturation pressure, leading to the following boundary condition for the vapor mass fraction:

$$k|_{r=R} = \left[1 + \frac{\mathcal{R}_v}{\mathcal{R}_g}\left(\frac{p_b}{p_{v,sat}(T_\infty)} - 1\right)\right]^{-1}, \quad (26)$$

where $p_{v,sat}(T) = p_{ref}\exp(-T_{ref}/T)$ is the temperature-dependent saturation pressure of the water vapor with empirical constants p_{ref} and T_{ref}[43]. Quantitative values for p_{ref}, T_{ref}, and T_∞ used in this study are included in Table 2.

Regarding the initial conditions for the bubble contents, for both LIC and UIC, we assume that the bubble contents are in thermal equilibrium at $t = 0$. Accordingly, the initial temperature field is spatially constant and given by $T(r, t = 0) = T_\infty$. Likewise, the water vapor partial pressure field is taken to be spatially constant and given through its saturation pressure at the ambient temperature, so that the initial vapor mass fraction field $k(r, t = 0)$ is also spatially constant and given by Eq. (26). Finally, following the arguments in Estrada *et al.*[21], for LIC, the initial bubble pressure is

$$p_b(t=0) = p_{v,sat}(T_\infty) + \left(p_\infty + \frac{2\gamma}{R_0} - p_{v,sat}(T_\infty)\right)\left(\frac{R_0}{R_{max}}\right)^3. \quad (27)$$

For UIC, the initial bubble pressure is $p_b(t = 0) = p_\infty + 2\gamma/R_0$.

Prior to obtaining numerical solutions, the governing equations for the bubble contents are non-dimensionalized as discussed in Estrada *et al.*[21], which for brevity, are not recapitulated here. Then, regarding the spatial discretization of the PDEs (22) and (23), the spatial derivatives are calculated using second-order central differences on a grid of $N + 1$ equidistant points inside the bubble[50]. In this study, we use $N = 500$. The method of time evolution for the governing equations for the bubble contents differs between the KM-based approach and the FE-based approach. For KM-based numerical solutions, the discretized governing equations for the bubble contents are evolved forward in time in conjunction with the KM equation (16) using a variable-step, variable-order solver (MATLAB `ode15s`). For FE-based numerical solutions, within a FE time increment, the displacement field in the surroundings, and hence the bubble radius, is updated explicitly using the explicit central difference scheme, and then, the discretized governing equations for the bubble contents are evolved forward in time using the fourth-order Runge-Kutta method. When the governing equations for the bubble contents require a stable time step that is smaller than the stable time increment required for the FE update, the discretized governing equations for the bubble contents are evolved forward in time using a number of substeps, in which the bubble radius is linearly interpolated over the course of the FE time increment.

References

1 M. K. Nyein, A. M. Jason, L. Yu, C. M. Pita, J. D. Joannopoulos, D. F. Moore and R. A. Radovitzky, *Proceedings of the National Academy of Sciences*, 2010, **107**, 20703–20708.

2 R. M. Wright, A. Post, B. Hoshizaki and K. T. Ramesh, *Journal of Neurotrauma*, 2013, **30**, 102–118.

3 R. W. Carlsen, A. L. Fawzi, Y. Wan, H. Kesari and C. Franck, *Brain Multiphysics*, 2021, **2**, 100024.

4 J. B. Estrada, H. C. Cramer III, M. T. Scimone, S. Buyukozturk and C. Franck, *Brain Multiphysics*, 2021, **2**, 100034.

5 E. Vlaisavljevich, K. W. Lin, M. Warnez, R. Singh, L. Mancia, A. Putnam, E. Johnsen, C. Cain and Z. Xu, *Physics in Medicine & Biology*, 2015, **60**, 2271–2292.

6 L. Mancia, E. Vlaisavljevich, Z. Xu and E. Johnsen, *Ultrasound in Medicine and Biology*, 2017, **43**, 1421–1440.

7 L. Mancia, E. Vlaisavljevich, N. Yousefi, M. Rodriguez, T. J. Ziemlewicz, F. T. Lee, D. Henann, C. Franck, Z. Xu and E. Johnsen, *Physics in Medicine & Biology*, 2019, **64**, 225001.

8 E.-A. Brujan and A. Vogel, *Journal of Fluid Mechanics*, 2006, **558**, 281–308.

9 M. S. Hutson and X. Ma, *Physical Review Letters*, 2007, **99**, 158104.

10 Y. Hu, J.-O. You, D. T. Auguste, Z. Suo and J. J. Vlassak, *Journal of Materials Research*, 2012, **27**, 152?160.

11 J. A. Zimberlin, N. Sanabria-DeLong, G. N. Tew and A. J. Crosby, *Soft Matter*, 2007, **3**, 763–767.

12 S. Kundu and A. J. Crosby, *Soft Matter*, 2009, **5**, 3963–3968.

13 S. Raayai-Ardakani, Z. Chen, D. R. Earl and T. Cohen, *Soft Matter*, 2019, **15**, 381–392.

14 S. Raayai-Ardakani and T. Cohen, *Extreme Mechanics Letters*,

2019, **31**, 100536.
15 S. Chockalingam, C. Roth, T. Henzel and T. Cohen, *Journal of the Mechanics and Physics of Solids*, 2021, **146**, 104172.
16 D. Richler and D. Rittel, *Experimental Mechanics*, 2014, **54**, 805–815.
17 Y. Toyoda and Y. Gupta, *Journal of Applied Physics*, 2014, **116**, 153512.
18 M. P. Milner and S. B. Hutchens, *Extreme Mechanics Letters*, 2019, **28**, 69–75.
19 D. Veysset, Y. Sun, J. Lem, S. Kooi, A. Maznev, S. Cole, R. Mrozek, J. Lenhart and K. Nelson, *Experimental Mechanics*, 2020, **60**, 1179–1186.
20 X. G. Tan, Y. Chen and T. J. O'Shaughnessy, *Journal of the Mechanical Behavior of Biomedical Materials*, 2022, **133**, 105293.
21 J. B. Estrada, C. Barajas, D. L. Henann, E. Johnsen and C. Franck, *Journal of the Mechanics and Physics of Solids*, 2018, **112**, 291–317.
22 J. Yang, H. C. Cramer III and C. Franck, *Extreme Mechanics Letters*, 2020, **39**, 100839.
23 L. Mancia, J. Yang, J.-S. Spratt, J. R. Sukovich, Z. Xu, T. Colonius, C. Franck and E. Johnsen, *Soft Matter*, 2021, **17**, 2931–2941.
24 J.-S. Spratt, M. Rodriguez, K. Schmidmayer, S. H. Bryngelson, J. Yang, C. Franck and T. Colonius, *Journal of the Mechanics and Physics of Solids*, 2021, **152**, 104455.
25 J. Yang, H. C. Cramer III, E. C. Bremer, S. Buyukozturk, Y. Yin and C. Franck, *Extreme Mechanics Letters*, 2022, **51**, 101572.
26 C. W. Barney, C. E. Dougan, K. R. McLeod, A. Kazemi-Moridani, Y. Zheng, Z. Ye, S. Tiwari, I. Sacligil, R. A. Riggleman, S. Cai, J.-H. Lee, S. R. Peyton, G. N. Tew and A. J. Crosby, *Proceedings of the National Academy of Sciences*, 2020, **117**, 9157–9165.
27 S. Buyukozturk, J.-S. Spratt, D. Henann, T. Colonius and C. Franck, *Experimental Mechanics*, 2022, **62**, 1–14.
28 C. T. Wilson, T. L. Hall, E. Johnsen, L. Mancia, M. Rodriguez, J. E. Lundt, T. Colonius, D. L. Henann, C. Franck and Z. Xu, *Physical Review E*, 2019, **99**, 043103.
29 L. Mancia, M. Rodriguez, J. Sukovich, Z. Xu and E. Johnsen, *Physics in Medicine & Biology*, 2020, **65**, 225014.
30 R. Gaudron, M. T. Warnez and E. Johnsen, *Journal of Fluid Mechanics*, 2015, **766**, 54–75.
31 M. Warnez and E. Johnsen, *Physics of Fluids*, 2015, **27**, 063103.
32 J. C. Luo, H. Ching, B. G. Wilson, A. Mohraz, E. L. Botvinick and V. Venugopalan, *Scientific reports*, 2020, **10**, 1–13.
33 S. Tiwari, A. Kazemi-Moridani, Y. Zheng, C. W. Barney, K. R. McLeod, C. E. Dougan, A. J. Crosby, G. N. Tew, S. R. Peyton, S. Cai and J.-H. Lee, *Soft Matter*, 2020, **16**, 9006–9013.
34 M. Plesset, *Journal of Applied Mechanics*, 1949, **16**, 277–282.
35 C. E. Brennen, *Cavitation and Bubble Dynamics*, 1995.
36 J. Keller and M. Miksis, *The Journal of the Acoustical Society of America*, 1980, **68**, 628–633.
37 S. Reese and S. Govindjee, *International Journal of Solids and Structures*, 1998, **35**, 3455–3482.
38 A. Kumar and O. Lopez-Pamies, *Comptes Rendus Mecanique*, 2016, **344**, 102–112.
39 J. K. Knowles, *International Journal of Fracture*, 1977, **13**, 611–639.
40 L. Anand, N. M. Ames, V. Srivastava and S. A. Chester, *International Journal of Plasticity*, 2009, **25**, 1474–1494.
41 R. Nigmatulin, N. Khabeev and F. Nagiev, *International Journal of Heat and Mass Transfer*, 1981, **24**, 1033–1044.
42 I. Akhatov, O. Lindau, A. Topolnikov, R. Mettin, N. Vakhitova and W. Lauterborn, *Physics of Fluids*, 2001, **13**, 2805.
43 C. Barajas and E. Johnsen, *The Journal of the Acoustical Society of America*, 2017, **141**, 908–918.
44 A. Prosperetti and A. Lezzi, *Journal of Fluid Mechanics*, 1986, **168**, 457–478.
45 J. Lysmer and R. L. Kuhlemeyer, *Journal of the Engineering Mechanics Division*, 1969, **95**, 859–877.
46 E. Vlaisavljevich, K. W. Lin, A. Maxwell, M. Warnez, L. Mancia, R. Singh, A. Putnam, J. B. Fowlkes, E. Johnsen, C. Cain and Z. Xu, *Ultrasound in Medicine and Biology*, 2015, **41**, 1651–1667.
47 J. Yang, A. Tzoumaka, K. Murakami, E. Johnsen, D. L. Henann and C. Franck, *Physical Review E*, 2021, **104**, 045108.
48 P. Movahed, W. Kreider, A. D. Maxwell, S. B. Hutchens and J. B. Freund, *The Journal of the Acoustical Society of America*, 2016, **140**, 1374–1386.
49 V. Kamath, A. Prosperetti and F. Egolfopoulos, *The Journal of the Acoustical Society of America*, 1993, **94**, 248–260.
50 A. Prosperetti, L. A. Crum and K. W. Commander, *The Journal of the Acoustical Society of America*, 1988, **83**, 502–514.